Influence of Mo alloying on the thermal stability and hardness of ultrafine-grained Ni processed by high-pressure torsion

Garima Kapoor[a], Yi Huang[b], V. Subramanya Sarma[c], Terence G. Langdon[b], Jenő Gubicza[a*]

[a]Department of Materials Physics, Eötvös Loránd University, P.O.B.32, Budapest, H-1518, Hungary
[b]Materials Research Group, Faculty of Engineering and the Environment, University of Southampton, Southampton SO17 1BJ, UK
[c]Department of Metallurgical and Materials Engineering, Indian Institute of Technology Madras, Chennai 600036, India

[*]Corresponding author: Tel: + 36-1-372-2876, Fax: +36-1-372-2811, e-mail: jeno.gubicza@ttk.elte.hu

Abstract

The influence of Mo alloying on the thermal stability of grain size, dislocation density and hardness of ultrafine-grained (UFG) Ni alloys was studied. The UFG microstructure in alloys with low (~0.3 at.%) and high (~5 at.%) Mo contents was achieved by high-pressure torsion (HPT) performed for 20 turns at room temperature. The thermal stability of the two alloys was studied by calorimetry. A Curie-transition from ferromagnetic to paramagnetic state was not found for the Ni-5% Mo alloy due to the high Mo content. It was found that heating at a rate of 40 K/min up to ~850 K resulted in a complete recovery and recrystallization of the UFG microstructure in the alloy with 0.3% Mo. The same annealing for Ni-5% Mo led only to a moderate reduction of the dislocation density and the grain size remained in the UFG regime. Therefore, the higher Mo content yielded a much better thermal stability of the Ni alloy. The influence of the change of the microstructure during annealing on the hardness is discussed.

Keywords: high-pressure torsion; Ni-Mo alloys; dislocations; grain size; hardness; thermal stability

1. Introduction

Ni-Mo alloys possess high hardness and wear resistance which make them useful for various practical applications. For instance, these alloys can be used as hard coating materials [1]. In addition, they exhibit corrosion resistance to the reducing acids, such as hydrogen chloride. Thus, Ni-Mo alloys can be used as catalysts in the production of hydrogen as these acids induce reducing reactions and generally result in hydrogen evolution at cathodic sites [2-4]. These alloys also show high activity and long-term stability as hydrogen evolution reaction catalysts under alkaline conditions. They are also applicable as substrate material for superconducting coatings which can be produced by severe cryorolling and subsequent annealing [5]. The latter processing provides extremely sharp cube texture as required for epitaxial coatings.

Improvement in the mechanical properties of Ni-Mo alloys can be attained by the implementation of efficient and novel severe plastic deformation processes, such

as equal-channel angular pressing (ECAP), cryorolling or high-pressure torsion (HPT). Over the years, there is an increasing interest in employing SPD techniques for production of ultrafine-grained (UFG) materials [6-11]. HPT is considered as the most effective SPD method in grain refinement and improvement of the strength of metallic materials [12-17]. The enhanced properties of UFG microstructures can be degraded due to grain growth at elevated temperatures [18-22]. The stability of UFG microstructures is an important aspect for their reliable performance in practical applications. Thus, a study of microstructure stability of UFG materials by annealing to high temperatures is crucial.

The addition of alloying elements further influences the development of the UFG microstructures during SPD as well as their thermal stability. Solute atoms have pinning effects on lattice defects, such as dislocations and grain boundaries, therefore they can stabilize the UFG microstructure [23-28]. The influence of concentrations of alloying elements on the thermal stability of face-centered cubic (fcc) metals (e.g., Ni and Cu) processed by SPD has been investigated in the literature [29,30]. However, despite the significant possible applications of Ni-Mo alloys, no investigations have been conducted to date to examine the influence of annealing on the microstructure and properties of HPT-deformed Ni-Mo alloys. Therefore, the present study was initiated to study the influence of heat-treatment on the microstructure and mechanical properties of UFG Ni alloys with two different Mo concentrations. The samples processed by a two-step combination of cryorolling and 20 turns of HPT were annealed to about 850 K and the microstructural parameters were compared with the HPT-processed state. In addition, the variation of the hardness during annealing was examined and correlated to the change of microstructure.

2. Experimental material and procedures

2.1. Processing of UFG Ni-Mo alloys

Two Ni alloys with low and high Mo contents were processed by induction melting and casting into a Cu-mould. The chemical compositions of the as-processed Ni alloys were determined by energy dispersive spectroscopy (EDS) in a scanning electron microscope (SEM). The alloys with ~0.28 and ~5.04 at.% of Mo were labelled as Low-Mo and High-Mo, respectively. Although, in addition to Mo other elements, such as Al (0.84-1.08 at.%) , Fe (0.13-0.25 at.%) and Si (0.05-0.34 at.%) were also found in the samples, the major difference between the chemical compositions of the two samples was the much higher Mo content in the material labelled as High-Mo. Detailed chemical compositions for Low-Mo and High-Mo alloys were given earlier [31]. The as-cast ingots with diameters of ~32 mm were hot-rolled at 1100 °C to a thickness of ~13 mm. The hot-rolled samples were then subjected to a combination of cryorolling and HPT. First, small strips cut from the hot-rolled materials were processed by cryorolling at liquid nitrogen temperature (LNT). This procedure resulted in a reduction of the thickness from ~13 mm to ~3 mm in multiple passes with a reduction of ~5% per pass. Then, disks with diameters of ~10 mm and thicknesses of ~1 mm were prepared from the cryorolled materials. In the second step of SPD, the sample was processed by the HPT technique under quasi-constrained conditions [32] with an applied pressure of 6.0 GPa and a rotating speed of 1 rpm at RT for 20 turns.

2.2. Differential scanning calorimetry

Our former study [31] revealed that for both alloys the microstructural parameters and the hardness were saturated between the half-radius and the periphery of the disks processed by 20 turns of HPT. Therefore, the thermal stability of the microstructures was investigated in the region between the half radius and periphery of the disks using differential scanning calorimetry (DSC). The DSC experiments were conducted on small samples cut from these regions of the HPT disks by a Perkin Elmer (DSC2) calorimeter at a heating rate of 40 K/min under an Ar atmosphere. Then, the HPT-processed samples were heated up to a characteristic temperature of the DSC thermograms. These specimens are regarded as annealed samples.

2.3. Microstructure from EBSD

The microstructures of the HPT-processed and the annealed Ni alloys were studied by electron backscatter diffraction (EBSD) using an FEI Quanta 3D SEM. Before EBSD, the specimens were mechanically polished first by SiC abrasive papers with 600, 1200, 2500 and 4000 grit and then by a colloidal silica suspension (OP-S) having a particle size of 1 micrometer. After mechanical polishing, the surfaces were treated by electro-polishing at 28 V and 1 A using an electrolyte with a composition of 70% ethanol, 20% glycerine and 10% perchloric acid (in vol. %). The step size in the EBSD study was ~30 nm and the grain sizes were evaluated using Orientation Imaging Microscopy (OIM) software. It is noted that only those regions in the EBSD images which were bounded by high-angle grain boundaries (HAGBs) with misorientations higher than 15° were considered as grains.

The distortions inside the grains were analysed using Kernel Average Misorientation (KAM) maps prepared by the OIM software. In this evaluation process, a local misorientation angle value was assigned to each pixel which was determined as the average misorientation between the studied central pixel and all pixels at the perimeter of the kernel around the investigated pixel. The radii of the kernels were ~50 nm for all images even if their pixel sizes were smaller in order to make their KAM maps comparable.

2.4. Characterization of microstructure by X-ray diffraction

The phase composition and the microstructural parameters were investigated by X-ray diffraction (XRD). The Debye–Scherrer diffraction rings were detected on two dimensional imaging plates using a high-resolution diffractometer (Multimax-9 made by Rigaku) with $CuK\alpha_1$ radiation (wavelength: $\lambda = 0.15406$ nm). The X-ray line profile analysis (XLPA) was carried out with the Convolutional Multiple Whole Profile (CMWP) fitting method in order to determine the dislocation density [33]. In this fitting procedure, the diffraction pattern is fitted by the sum of a background spline and the convolution of the instrumental pattern and the theoretical line profiles related to dislocations, crystallite size and planar faults. As an example, Fig. 1 shows the CMWP fitting for the High-Mo sample processed by 20 turns of HPT. The open circles and solid line represent the measured and fitted patterns, respectively.

2.5. Microhardness testing

The Vickers microhardness of the HPT-processed and the annealed samples was measured using a Zwick Roell ZHμ hardness tester with an applied load of 0.5 kg and a dwell time of 10 s for both compositions of Ni alloys.

3. Experimental results

Illustrative EBSD images for the HPT-processed microstructures of both alloys were presented in our previous study [36]. Figs. 2 and 3 show the grain sizes and the dislocation densities for Low-Mo and High-Mo samples obtained immediately after 20 turns of HPT. The grain size of the HPT-processed High-Mo alloy was smaller (~130 nm) than the value obtained for the Low-Mo sample (~184 nm). In addition, the dislocation density was about two times higher (~23 × 10^{14} m^{-2}) for the former material than for the latter specimen (~60 × 10^{14} m^{-2}). The higher dislocation density and the smaller grain size for the HPT-processed High-Mo alloy can be attributed to the hindering effect of Mo atoms on the annihilation of dislocations and the motion of grain boundaries during deformation.

Fig. 4a and b show the DSC thermograms obtained at 40 K/min for the HPT-processed Low-Mo and High-Mo samples, respectively. For both materials, the first and the second heating scans are also shown. For the Low-Mo material, an endothermic peak was observed for both scans with a peak temperature of ~627 K. This peak is related to the Curie-transition from ferromagnetic to paramagnetic state. Between ~600 and ~830 K, the heat flow for the first heating scan is considerably larger than for the second scan, indicating exothermic processes. The maximum of this endothermic peak can be found at ~743 K. This peak corresponds to the recovery and/or recrystallization of the UFG microstructure in the HPT-processed Low-Mo alloy, as shown in the next paragraph. For the High-Mo material, the endothermic peak related to the ferromagnetic to paramagnetic transition was not observed. However, a long exothermic peak was detected between ~630 and ~1000 K. The peak maximum can be found at about 786 K. The characteristic temperatures of the DSC thermograms are listed in Table 1.

In order to characterize the difference between the thermal stability of the HPT-processed Low-Mo and High-Mo alloys, additional samples were heated up to ~850 K at 40 K/min and then quenched to RT. This temperature was selected as above so that there is no exothermic signal for the Low-Mo alloy (see Fig. 4a). The grain size and the dislocation density of the annealed Low-Mo and High-Mo samples were determined by EBSD and XLPA, respectively. Fig. 5a and b show inverse pole figure (IPF) maps obtained by EBSD for the annealed Low-Mo and High-Mo alloys, respectively. The HAGBs and the LAGBs are indicated by black and white lines, respectively. The grain size of the annealed samples determined from the IPF maps are shown in Fig. 2. For the Low-Mo material, the average grain size increased from ~184 to ~874 nm while in the case of the High-Mo sample the grain size was enhanced from ~130 only to ~225 nm. In addition, for the Low-Mo sample most of the boundaries are straight and there are no orientation gradients in the grains which indicate that the lattice distortion is negligible. The KAM maps in Figs. 5c and d show the local misorientations between 0 and 5° for the HPT-processed Low-Mo and High-Mo alloys after annealing at ~850 K. The KAM maps are indicative of local strains in the studied microstructures. It can be seen that for the annealed Low-Mo alloy considerable local misorientations may be observed only in the vicinity of some grain boundaries.

These results suggest that the microstructure in the Low-Mo alloy was recrystallized during annealing and this is supported by the practically zero dislocation density. In fact, XLPA evaluation could not be performed for the annealed Low-Mo sample as the peak breadth was as narrow as the instrumental profile. Thus, the dislocation density in this material was lower than the detection limit for the applied diffractometer configuration (~10^{13} m^{-2}). The Debye-Scherrer ring for reflection *220* of the annealed Low-Mo specimen is shown in Fig. 6a. The spotty ring also suggests that the sample exhibits a recrystallized microstructure. Each high intensity spot is scattered from a recrystallized grain. Fig. 6b shows that the Debye-Scherrer ring for the annealed High-Mo alloy is homogeneous which indicates that this sample was not recrystallized at ~850 K. The dislocation density in High-Mo decreased from ~60 × 10^{14} m^{-2} to ~19 × 10^{14} m^{-2} so that only a moderate recovery occurred during annealing. This is confirmed by the KAM map in Fig. 5d which reveals high lattice distortion inside the grains even after annealing at ~850 K. It is noted that in the Low-Mo alloy the recrystallization also resulted in an elongated shape for many grains (see Fig. 5a) since the nucleated new grains are preferably separated from the parent grains by low energy boundaries growing only on specific crystallographic planes (e.g., twin boundaries on planes {111}). At the same time, in the annealed High-Mo alloy the grain shape remained equiaxial due to the lack of recrystallization (see Fig. 5b).

The higher thermal stability of the High-Mo alloy is also reflected in the variation of hardness during annealing (see Fig. 7). While the hardness decreased considerably from ~3300 to ~1340 MPa during annealing of the HPT-processed Low-Mo alloy, a significant change in the very high hardness of ~4320 MPa for the High-Mo specimen was not observed. The reduction of the hardness for Low-Mo can be explained by the considerable decrease in the dislocation density and the grain-growth that occurred due to recrystallization (see Figs. 2 and 3). For the High-Mo sample, the much lower decrease of the dislocation density and the moderate increase of the grain size suggests a lower reduction of the hardness. Therefore, the practically unchanged hardness for the High-Mo alloy is surprising and seems to be in contradiction with the changes of the microstructure. However, this effect can be explained by the plastic deformation occurring during the hardness measurement, as discussed in the next section.

4. Discussion

Fig. 4 shows that while the Curie temperature for Low-Mo was detected as ~627 K, in the case of the High-Mo alloy an endothermic signal for a ferromagnetic to paramagnetic transition was not observed. This observation is in line with former studies which indicated that the Curie temperature of Ni significantly decreased with increasing Mo content [34]. The literature data in [34] show that for ~5 at.% (8 wt.%) Mo alloying there was a reduction of Curie temperature to 333 K, therefore the paramagnetic transition cannot be observed in the present experiments starting at 300 K, due to the transient DSC signal in the beginning of the measurements. The Curie temperature for Low-Mo (~627 K) agrees with the value characteristic for pure Ni, so that the low Mo content of 0.3 at.% has no considerable effect on the ferromagnetic-paramagnetic transition.

Our study demonstrates that the thermal stability of the present HPT-processed UFG Ni alloys is strongly influenced by the Mo content. While the Low-Mo material fully recrystallized at ~850 K, in the High-Mo alloy only a partial recovery and

a moderate grain growth were observed. With increasing Mo concentration, the exothermic DSC peak related to recovery and recrystallization was shifted to a higher temperature. Moreover, while this peak ends at ~850 K for the Low-Mo sample, the heat release finishes only at ~1000 K for the High-Mo alloy. The much better thermal stability of the HPT-processed UFG microstructure for the High-Mo material can be attributed to the retarding effect of the Mo solute atoms on the motion of dislocations and grain boundaries which are necessary for recovery and recrystallization. In addition, former studies (e.g., [35]) have shown that the segregation of alloying elements on grain boundaries may reduce the energy of boundaries, thereby reducing the driving force for recrystallization and grain growth. As a consequence, the segregation of solute atoms can stabilize UFG microstructures.

Although the higher Mo content resulted in a much better thermal stability, the dislocation density decreased to about half of the value achieved after HPT and the grain size also increased by about 50% during annealing. Therefore, it was a surprising result that the hardness remained practically unchanged despite the recovery and grain growth. This phenomenon can be understood if we consider the influence of the hardness measurement on the probed material. Namely, during hardness testing a probe tip is pressed into the material which results in a plastic deformation around the indent. During this plastic deformation, dislocations are generated so that the hardness value characterizes this strain hardened material. The equivalent plastic strain corresponding to the hardness measurement with a Vickers or Berkovich indenter is about 8% [36]. Therefore, the hardness value is related to the flow stress at a plastic strain of 8% and not to the yield strength of the material before hardness testing. For severely deformed metallic materials, the strain hardening is usually low and therefore the difference between the yield strength and the flow stress at a plastic strain of 8% is very small. Thus, for these specimens the hardness value can be related to the yield strength. At the same time, for annealed samples the strain hardening is usually large and therefore the difference between the yield strength and the flow stress at a plastic strain of 8% is significant. As a consequence, in the latter cases the hardness cannot be related directly to the annealed microstructure. In the present study, for the High-Mo sample the annealing must have resulted in a decrease of the yield strength due to recovery and grain growth. However, the flow stress at a plastic strain of 8% may be considerably larger than the yield strength so that the hardness cannot reflect the change in the microstructure during annealing. In addition, besides the density of dislocations, their arrangement has also an influence on the dislocation strengthening effect. Specifically, a more clustered dislocation structure is usually associated with a larger strengthening effect for the same dislocation density [37,38]. XLPA evaluation also determines parameter M which reflects the arrangement of the dislocations. A smaller value of M relates to a more shielded strain field of the dislocations, and the arrangement of dislocations into low energy configurations, such as LAGBs or dipoles, yields a consequent decrease in M. The present experiments show that for the HPT-processed High-Mo alloy the value of M decreased from ~4.8 ± 0.5 to ~1.6 ± 0.2 during annealing up to ~850 K. The more clustered dislocation structure after annealing decreases the softening effect of the reduced dislocation density. Most probably, this effect and the strain hardening caused by the hardness testing resulted in the unchanged hardness after annealing.

5. Summary and conclusions

The influence of Mo content on the thermal stability of UFG microstructures in Ni alloys processed by HPT was studied. The following conclusions were drawn:

1. The exothermic peak observed in the DSC thermograms was shifted to a higher temperature with increasing Mo content. For a Low-Mo alloy, this peak finished at ~830 K while for a High-Mo material the exothermic processes, such as recovery and recrystallization, end only at ~1000 K. In addition, alloying with ~0.3 at.% Mo in Ni had only a negligible effect on the Curie temperature, while for ~5 at.% Mo a ferromagnetic-paramagnetic transition was not observed in the studied temperature range.
2. Annealing up to ~850 K resulted in a full recrystallization of the UFG microstructure in the Low-Mo alloy. In this process, the grain size increased from ~184 to ~874 nm while the dislocation density decreased from ~23 × 10^{14} m^{-2} below 10^{13} m^{-2}. At the same time, for the High-Mo material only a partial recovery and moderate grain growth was observed. In this material, the dislocation density decreased from ~60 × 10^{14} m^{-2} to ~19 × 10^{14} m^{-2} and the grain size increased from ~130 to ~225 nm. The better thermal stability of the High-Mo alloy can be attributed to the pinning effect of Mo solute atoms on dislocations and grain boundaries which retards their motion during recovery and recrystallization. In addition, the segregation of Mo at grain boundaries reduces the boundary energy, thereby decreasing the thermodynamical driving force for recrystallization and grain-growth.
3. The hardness for the Low-Mo alloy considerably decreased from ~3300 to ~1340 MPa due to recrystallization during annealing. At the same time, the partial recovery and the moderate grain growth failed to yield significant hardness reduction for the High-Mo material. This phenomenon can be explained partly by the clustering of dislocations into a more dense structure as revealed by the reduced dislocation arrangement parameter. In addition, the hardness measurement causes a plastic deformation around the indenter which results in strain hardening in the annealed sample.

Acknowledgments

This research was presented at the 3rd Pan American Materials Congress held as part of the TMS Annual Meeting in San Diego, California, on February 27 - March 2, 2017. The authors are grateful to Mr. Alajos Ö. Kovács and Mr. Gábor Varga for DSC and EBSD investigations, respectively, This research was supported by the Hungarian Scientific Research Fund, OTKA, Grant no. K-109021. Two of the authors (YH and TGL) were supported by the European Research Council under ERC Grant Agreement No. 267464-SPDMETALS.

References

[1] Lehman EB, Bigos A, Indyka P, Kot M. Electrodeposition and characterization of nanocrystalline Ni-Mo coatings. Surface Coatings and Technology. 2011;211;67–71.

[2] Brown DE, Mahmood MN, Man MCM, Turner AK. Preparation and characterization of low overvoltage transition metal alloy electrocatalysts for hydrogen evolution in alkaline solutions. Electrochimica Acta. 1984;29;1551–1556.

[3] Schulz R, Huot JY, Trudeau ML, Bailey LD, Yan ZH, Jin S, et al. Nanocrystalline Ni-Mo alloys and their application in electrocatalysis. Journal of Materials Research. 1994;9;2998–3008.

[4] McKone JR, Sadtler BR, Werlang CA, Lewis NS, Gray HB. Ni−Mo nanopowders for efficient electrochemical hydrogen evolution. ACS Catal. 2013;3;166–169.

[5] Bhattacharjee PP, Ray RK, Upadhyaya A. Nickel base substrate tapes for coated superconductor applications. Journal of Materials Science. 2007;42;1984–2001.

[6] Koch CC. Top-down synthesis of nanostructured materials: mechanical and thermal processing methods. Reviews on advanced materials science. 2003;5(2);91–99.

[7] Zhilyaev AP, Kim BK, Szpunar JA, Baro MD, Langdon TG. The microstructural characteristics of ultrafine-grained nickel, Materials Science and Engineering A. 2005;391(1);377–389.

[8] Valiev RZ, Sabirov I, Zhilyaev AP, Langdon TG. Bulk nanostructured metals for innovative applications. JOM. 2012;64(10);1134–1142.

[9] Valiev RZ, Zhilyaev AP, Langdon TG. Bulk Nanostructured Materials: Fundamentals and Applications. 1st. ed. NJ: John Wiley & Sons, Inc, Hoboken; 2014.

[10] Valiev RZ, Estrin Y, Horita Z, Langdon TG, Zehetbauer MJ, Zhu Y. Producing bulk ultrafine-grained materials by severe plastic deformation. JOM. 2016;68(4);1216–1226.

[11] Zhilyaev AP, Gubicza J, Nurislamova G, Revesz A, Surinach S, Baro MD, Ungar T. Microstructural characteristics of ultrafine-grained nickel. Physica Status Solidi (a). 2005;198(2);263–271.

[12] Zhilyaev AP, Nurislamova GV, Kim BK, Baro MD, Szpunar JA, Langdon TG. Experimental parameters influencing grain refinement and microstructural evolution during high-pressure torsion. Acta Materialia. 2003;51(3);753–765.

[13] Hebesberger T, Stuwe HP, Vorhauer A, Wetscher F, Pippan R. Structure of Cu deformed by high pressure torsion. Acta Materialia. 2005;53(2);393–402.

[14] Zhilyaev AP, Langdon TG. Using high-pressure torsion for metal processing: fundamentals and applications. Progress in Materials Science. 2008;53(6);893–979.

[15] Hohenwarter A, Bachmaier A, Gludovatz B, Scheriau S, Pippan R. Technical parameters affecting grain refinement by high pressure torsion. International Journal of Materials Research. 2009;100(12);1653–1661.

[16] Wang YB, Ho JC, Cao Y, Liao XZ, Li HQ, Zhao YH, et al. Dislocation density evolution during high pressure torsion of a nanocrystalline Ni-Fe alloy, Applied Physics Letters; 2009;94(9);091911.
[17] Kawasaki M. Different models of hardness evolution in ultrafine-grained materials processed by high-pressure torsion. Journal of Materials Science. 2014;49(1);18–34.
[18] Gubicza J, Dobatkin SV, Khosravi E, Kuznetsov AA, Labar JL. Microstructural stability of Cu processed by different routes of severe plastic deformation. Materials Science and Engineering A. 2011;528;1828–1832.
[19] Alhamidi A, Edalati K, Horita Z, Hirosawa S, Matsuda K, Terada D. Softening by severe plastic deformation and hardening by annealing of aluminum–zinc alloy: significance of elemental and spinodal decompositions. Materials Science and Engineering A. 2014;610;17–27.
[20] Andreau O, Gubicza J, Zhang NX, Huang Y, Jenei P, Langdon TG. Effect of short-term annealing on the microstructures and flow properties of an Al-1% Mg alloy processed by high-pressure torsion, Materials Science and Engineering A. 2014;615;231–239.
[21] Bachmaier A, Hohenwarter A, Pippan R. New procedure to generate stable nanocrystallites by severe plastic deformation, Scripta Materialia 2009;61;1016-1019.
[22] Gubicza J. Defect Structure and Properties of Nanomaterials, 2nd. ed. Cambridge: Woodhead Publishing; 2017.
[23] Gubicza J, Chinh NQ, Horita Z, Langdon TG. Effect of Mg addition on microstructure and mechanical properties of aluminium. Materials Science and Engineering A. 387–389;2004;55–59.
[24] Gubicza J, Schiller I, Chinh NQ, Illy J, Horita Z, Langdon TG. The effect of severe plastic deformation on precipitation in supersaturated Al-Zn-Mg alloys. Materials Science and Engineering A. 2007;460–461;77–85.
[25] Qu S, An XH, Yang HJ, Huang CX, Yang G, Zang QS, et al. Microstructural evolution and mechanical properties of Cu–Al alloys subjected to equal channel angular pressing, Acta Materialia 2009;57;1586–1601.
[26] Liddicoat PV, Liao XZ, Zhao Y, Zhu Y, Murashkin MY, Lavernia EJ, et al. Nanostructural hierarchy increases the strength of aluminium alloys. Nature Communications. 2010;1 (Art. No. 63).
[27] Dopita M, Janecek M, Kuzel R, Seifert HJ, Dobatkin S. Microstructure evolution of CuZr polycrystals processed by high-pressure torsion. Journal of Materials Science. 2010;45;4631–4644.
[28] Kuzel R, Janecek M, Matej Z, Cizek J, Dopita M, Srba O. Microstructure of equal-channel angular pressed Cu and Cu-Zr samples studied by different methods. Metallurgical and Materals Transactions. A. 2010;41;1174–1190.
[29] Dobatkin SV, Gubicza J, Shangina DV, Bochvar NR, Tabachkov NU. High strength and good electrical conductivity in Cu-Cr alloys processed by severe plastic deformation. Materials Letters. 2015;153;5–9.
[30] Rathmayr GB, Pippan R, Influence of impurities and deformation temperature on the saturation microstructure and ductility of HPT-deformed. Acta Materialia. 2011;59;7228-7240.
[31] Kapoor G, Huang Y, Sarma VS, Langdon TG, Gubicza J. Effect of Mo addition on the microstructure and hardness of ultrafine-grained Ni alloys processed by a combination of cryorolling and high-pressure torsion. Materials Science and Engineering A. 2017;688;92–100.

[32] Figueiredo RB, Cetlin PR, Langdon TG. Using finite element modeling to examine the flow processes in quasi-constrained high-pressure torsion. Materials Science and Engineering A. 2011;528;8198-8204.
[33] Ribárik G, Gubicza J, Ungár T. Correlation between strength and microstructure of ball-milled Al–Mg alloys determined by X-ray diffraction. Materials Science and Engineering A. 2004;387–389;343–347.
[34] Karolus M, Lagiewka E. The structural studies on nanocrystalline Ni-Mo alloys after annealing, Proceedings of the XIX Conference of Applied Crystallography; 2003 September 1-4; Kraków, Poland. (Henryk Morawiec, Danuta Stróz; pp. 337-341, World Scientific, 2004).
[35] Millett PC, Selvam RP, Saxena A. Stabilizing nanocrystalline materials with dopants. Acta Materialia. 2007;55;2329–2336.
[36] Tabor D. The Hardness of Metals. 1st. ed. Oxford: Clarendon Press; 1951.
[37] Olivares FH, Sevillano JG. A quantitative assessment of forest-hardening in FCC metals. Acta Metallurgica. 1987;35;631-641.
[38] Gubicza J, Chinh NQ, Lábár JL, Dobatkin S, Hegedűs Z, Langdon TG. Correlation between microstructure and mechanical properties of severely deformed metals. Journal of Alloys and Compounds. 2009;483;271–274.

Figure and table captions

Figure 1: CMWP fitting of the X-ray diffraction pattern taken at the half radius of the High-Mo alloy disk processed by 20 turns of HPT. The open circles and the solid line represent the measured data and the fitted curve, respectively. The intensity is in a logarithmic scale.

Figure 2: Histogram of the grain sizes in the samples processed by 20 turns of HPT and the specimens annealed at ~850 K for both Low-Mo and High-Mo alloys.

Figure 3: Histogram of the dislocation densities in the samples processed by 20 turns of HPT and the specimens annealed at ~850 K for both Low-Mo and High-Mo alloys.

Figure 4: DSC thermograms obtained at a heating rate of 40 K/min for the regions between the half radius and the periphery of the disks processed by 20 turns of HPT for (a) Low-Mo and (b) High-Mo alloys.

Figure 5: IPF maps obtained by EBSD for the HPT-processed (a) Low-Mo and (b) High-Mo alloys after annealing at ~850 K. The color code for the maps is shown in the inset in (a). The HAGBs and the LAGBs are indicated by black and white lines, respectively. KAM maps showing the local misorientations between 0 and 5° for the HPT-processed (c) Low-Mo and (d) High-Mo alloys after annealing at ~850 K.

Figure 6: Debye-Scherrer rings for reflection *220* obtained for the HPT-processed (a) Low-Mo and (b) High-Mo alloys after annealing at ~850 K.

Figure 7: Histogram of the hardness values for the samples processed by 20 turns of HPT and the specimens annealed at ~850 K for both Low-Mo and High-Mo alloys.

Table 1: The characteristic temperatures of the thermograms obtained for the Low- and High-Mo alloys by DSC scan at 40 K/min. The Curie-temperature of the High-Mo alloy was taken from Ref. [34].

Fig. 1.

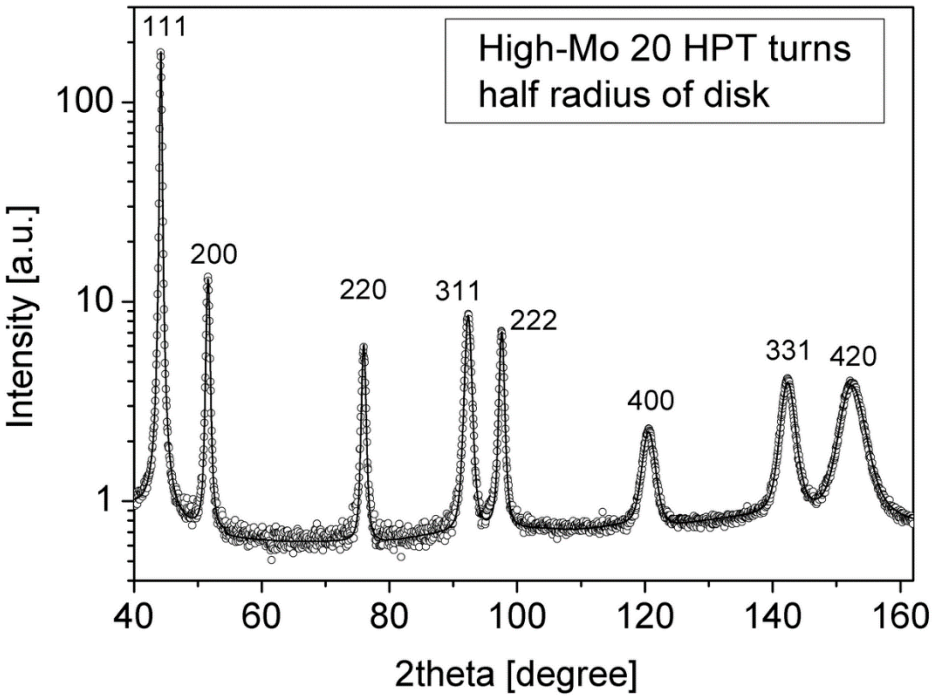
High-Mo 20 HPT turns
half radius of disk
111
200
220
311
222
400
331
420
Intensity [a.u.]
100
10
1
40
60
80
100
120
140
160
2theta [degree]

Fig. 2.

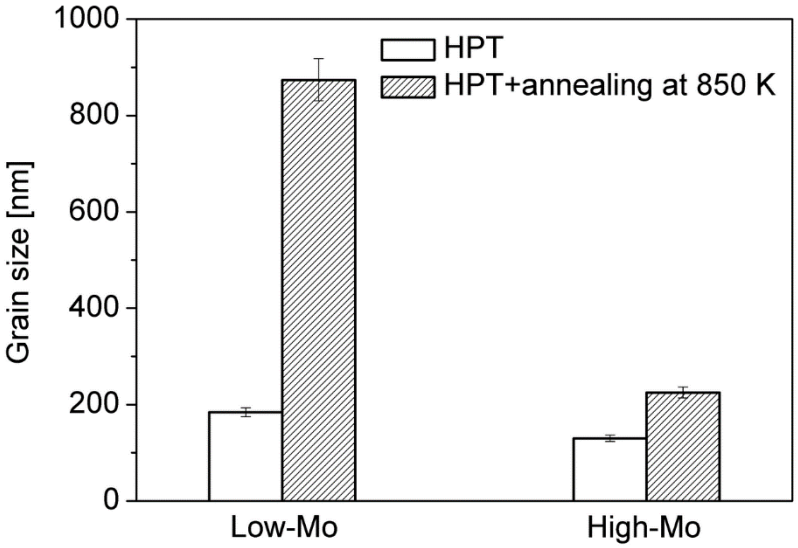
1000
800
600
400
200
0
Grain size [nm]
HPT
HPT+annealing at 850 K
Low-Mo
High-Mo

Fig. 3.

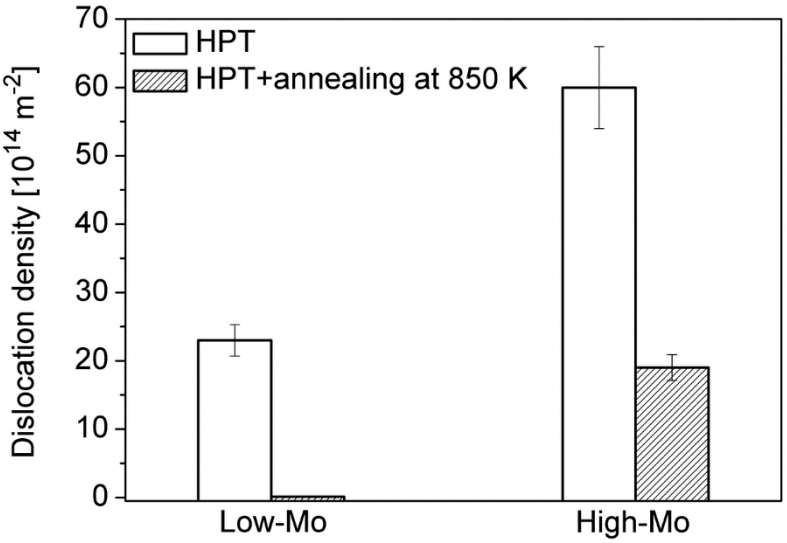
HPT
HPT+annealing at 850 K
Dislocation density [10^14 m^-2]
70
60
50
40
30
20
10
0
Low-Mo
High-Mo

Fig. 4.

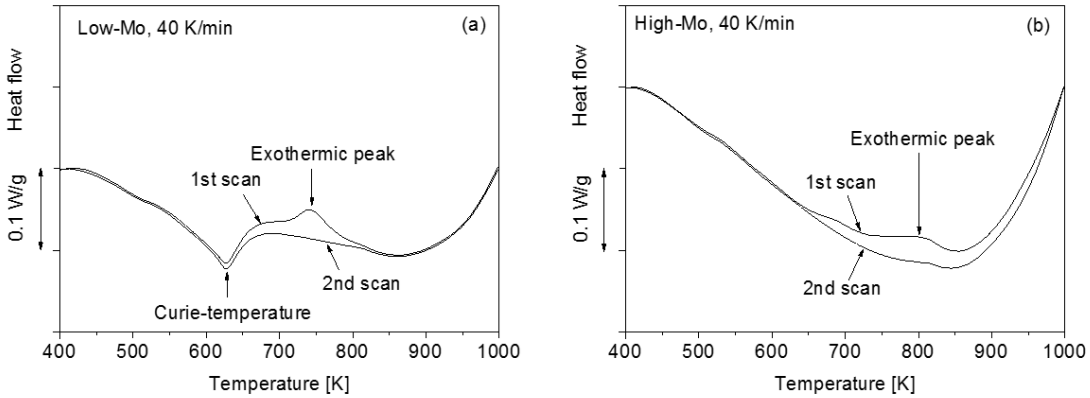
Low-Mo, 40 K/min
(a)
Heat flow
0.1 W/g
Exothermic peak
1st scan
2nd scan
Curie-temperature
400
500
600
700
800
900
1000
Temperature [K]
High-Mo, 40 K/min
(b)
Heat flow
0.1 W/g
Exothermic peak
1st scan
2nd scan
400
500
600
700
800
900
1000
Temperature [K]

Fig. 5.

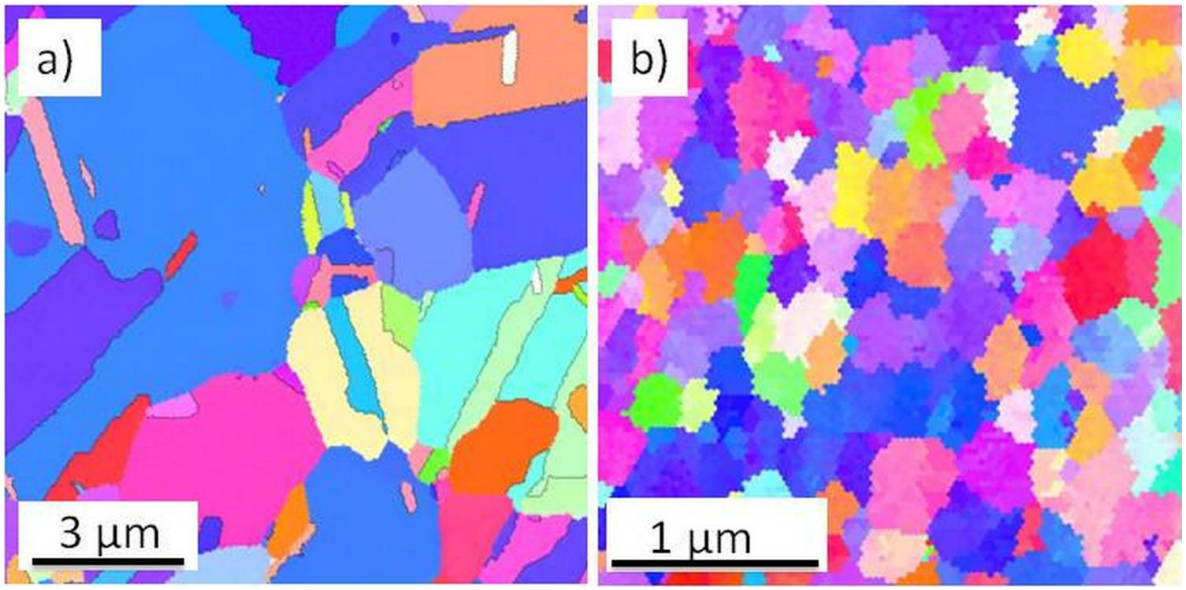

Fig. 6.

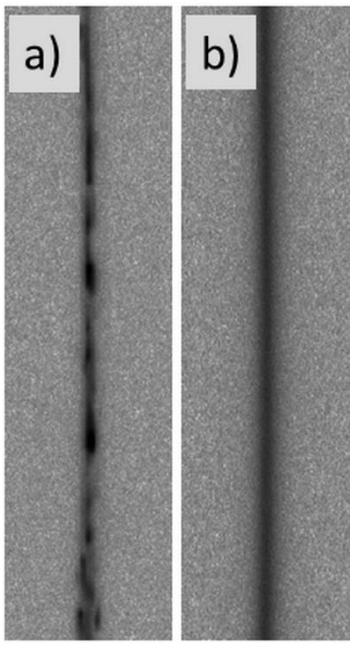

Fig. 7.

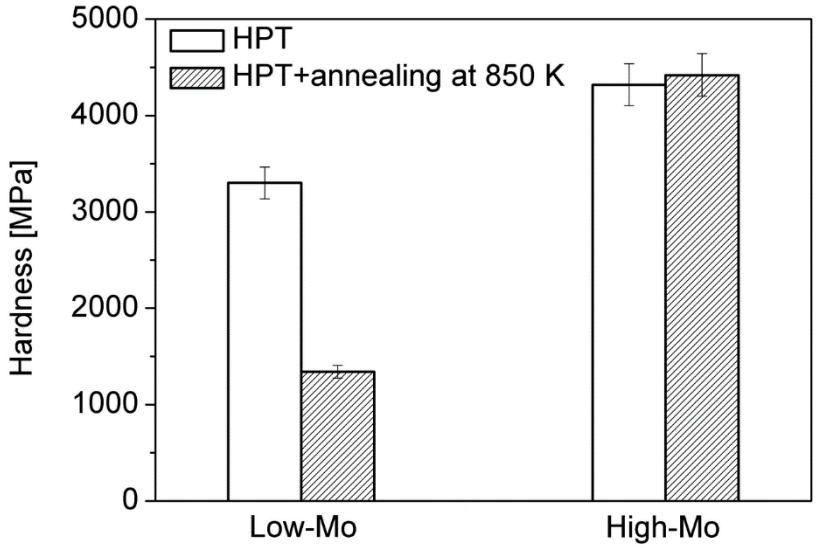
5000
4000
3000
2000
1000
0
Hardness [MPa]
HPT
HPT+annealing at 850 K
Low-Mo
High-Mo